ACS Energy LETTERS

http://pubs.acs.org/journal/aelccp

LETTER

Reversible Room-Temperature Fluoride-Ion Insertion in a Tunnel-Structured Transition Metal Oxide Host

Wasif Zaheer, Justin L. Andrews, Abhishek Parija, Forrest P. Hyler, Cherno Jaye, Conan Weiland, Young-Sang Yu, David A. Shapiro, Daniel A. Fischer, Jinghua Guo, Jesús M. Velázquez, and Sarbajit Banerjee*

Cite This: *ACS Energy Lett.* 2020, 5, 2520−2526

Read Online

ACCESS | Metrics & More | Article Recommendations | Supporting Information

ABSTRACT: An energy storage paradigm orthogonal to Li-ion battery chemistries can be conceptualized by employing anions as the primary charge carriers. F-ion conversion chemistries show promise but have limited cyclability as a result of the significant change in volume of active electrodes upon metal−metal fluoride interconversion. In contrast, the exploration of insertion chemistries has been stymied by the lack of hosts amenable to reversible F-ion insertion at room temperature. Here we show the reversible and homogeneous topochemical insertion/deinsertion and bulk diffusion of F ions within the one-dimensional tunnels of submicrometer-sized $FeSb_2O_4$ particles at room temperature. The insertion of F ions is evidenced by formal oxidation of the iron centers from Fe^{2+} to Fe^{3+} with a lattice volume contraction of <1% at a capacity of one F ion per iron center. The topochemical insertion of F ions is observed to be homogeneous across the $FeSb_2O_4$ particles. An approach to screen F-ion insertion electrodes through solution-phase topochemical methods is further demonstrated.

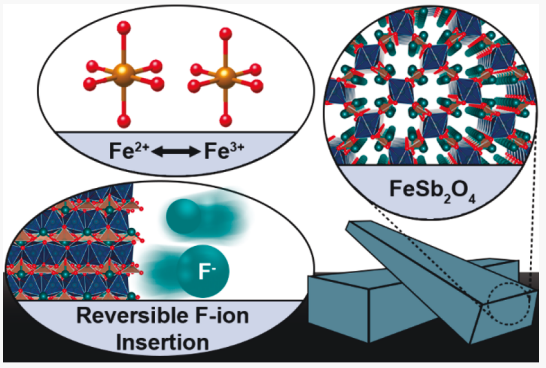

Li-ion batteries have emerged as the dominant energy storage paradigm for electromobility and consumer electronics applications.[1,2] However, with the demand for energy storage trending sharply upward across a diverse range of applications, there is increasing emphasis on not only conventional performance metrics such as energy and power density but also technological diversity, materials criticality, and the identification of energy storage concepts that satisfy the resource constraints and power needs of specific intended applications.[3] As such, substantial efforts have focused on the exploration of alternative "beyond lithium-ion" monovalent-ion (e.g., Na^+ and K^+) and multivalent-ion (e.g., Mg^{2+}, Ca^{2+}, and Al^{3+}) insertion and conversion battery chemistries.[4−7] An intriguing orthogonal energy storage paradigm can be conceptualized by employing anions as the primary charge carriers. In particular, F-ion conversion chemistries have recently attracted attention.[8−10] F-ion conversion batteries are predicated on the shuttling of F ions between metal and metal fluoride electrodes but show relatively poor cycle life as a result of the inevitably high entropy dissipation and large volume changes accompanying metal−metal fluoride conversion reactions.[11] In contrast, the insertion chemistry of F ions remains poorly developed; indeed, bulk solid-state diffusion of F ions at room temperature has not thus far been accomplished, representing a fundamental impediment to the realization of anion insertion batteries. In analogy with Li-ion batteries, F-ion insertion requires hosts with an abundance of interstitial sites, accessible redox centers, and the ability to accommodate the inserted ions without large lattice volume alteration; however, an important difference is that F-ion insertion reactions must bring about oxidation and not the reduction of the redox sites. Here, we demonstrate the reversible solution-phase insertion/deinsertion of F ions from a tunnel-structured p−d-block insertion host, $FeSb_2O_4$, at room temperature, evidencing the reversible oxidation/reduction of iron centers upon F-ion insertion/deinsertion. We demonstrate the unprecedented solid-state bulk diffusion of F ions at room temperature and use diffraction and synchrotron-based spectroscopy probes to

Received: June 21, 2020
Accepted: July 6, 2020
Published: July 6, 2020

https://dx.doi.org/10.1021/acsenergylett.0c01328
ACS Energy Lett. 2020, 5, 2520−2526

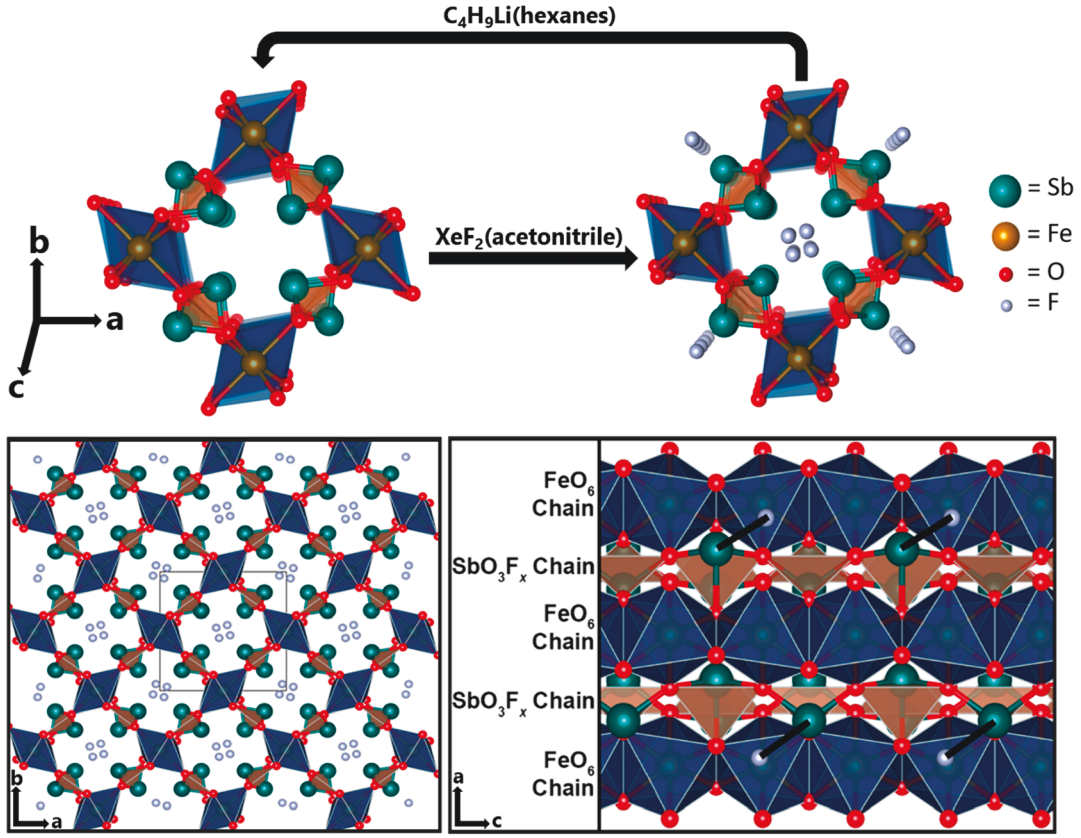

Figure 1. Reversible topochemical F-ion insertion in $FeSb_2O_4$. The depicted structures were obtained from Rietveld refinements shown in Figure S3, for the pristine and F-ion-inserted phases. The bottom panels highlight an expanded view along the *c* axis and a view down the crystallographic *b* axis, which shows chains of edge-sharing FeO_6 joined by corner-sharing SbO_3 trigonal pyramids.

characterize the distortion of the crystalline lattice, the crystallographic sites occupied by inserted F ions, and the modification of electronic structure resulting from F-ion insertion. As such, in addition to the novel functionality, we identify the key elements of atomistic and electronic structure necessary to overcome critical limitations of F-ion insertion batteries.

Challenges with F-ion diffusion have not only stymied the development of F-ion insertion batteries but also greatly limited the advancement of F-ion conversion chemistries. Grubbs and Jones demonstrated the operation of F-ion conversion electrodes at room temperature, but F-ion diffusion was confined to an ~8.4 nm surface layer.[12] As noted above, room-temperature F-ion insertion has not thus far been accomplished; F-ion insertion in redox active hosts has been constrained to high temperatures using solid electrolytes (>170 °C) or achieved using gas-phase reactions with F_2 gas at 230 °C.[13,14] A lack of understanding of fundamental mechanisms of F-ion insertion represents a key origin of the maturity gap between cation and anion insertion batteries. In this work, we have successfully demonstrated reversible room-temperature topochemical insertion of F ions into the quasi-one-dimensional tunnels of $FeSb_2O_4$. We further provide unambiguous characterization of the changes in average and local atomistic structure, demonstrating structural retention of the host lattice upon F-ion insertion/deinsertion at room temperature, and further identify specific interstitial lattice sites occupied by the inserted F ions. In addition to mapping the changes in the geometric structure, we also show quantitative changes in the oxidation states upon F-ion insertion and deinsertion. Finally, using scanning transmission X-ray microscopy imaging of hydrothermally synthesized micrometer-sized faceted $FeSb_2O_4$ particles, we provide evidence for bulk and not just surface diffusion of F ions within this system.[12]

The hydrothermally synthesized particles of $FeSb_2O_4$ exhibit a rodlike morphology and have been prepared as described in the Supporting Information by the reaction of Mohr's salt and $SbCl_3$ as per

$$FeSO_4(NH_4)_2SO_4{\cdot}6H_2O(aq) + 2SbCl_3(HCl) \xrightarrow[24\,h]{210\,^{\circ}C} FeSb_2O_4(s) + 2NH_3(g) + 2H_2SO_4(aq) + 6HCl(aq) + 2H_2O(l) \quad (1)$$

Figure 1 shows the structure of $FeSb_2O_4$ refined from the powder X-ray diffraction pattern shown in Figure 2A and Figure S3A and highlights the topochemical insertion and deinsertion of F ions as described here (*vide infra*). The solid product was obtained in ~78% yield with respect to the precursors. The diffraction data further attest to the phase purity of the hydrothermally prepared materials with no discernible crystalline impurities for the optimal synthetic conditions reported here. $FeSb_2O_4$ crystallizes in tetragonal space group $P4_2mbc$ ($a = b = 8.5807$ Å, and $c = 5.9131$ Å) and comprises edge-sharing FeO_6 octahedra bonded to corner-sharing SbO_3 tetrahedra with one vertex occupied by its lone pair of electrons (i.e., trigonal pyramidal local coordination environment). The resulting coordinative unsaturation of Sb opens up a large (4.14 Å diagonal), rigid one-dimensional channel along the [001] direction (further depicted in Figure S1). The lattice constants, atom positions, and refinement statistics are provided in Table S1. Figure S2 shows scanning electron microscopy (SEM) and transmission electron microscopy (TEM) images of the

https://dx.doi.org/10.1021/acsenergylett.0c01328
ACS Energy Lett. 2020, 5, 2520−2526

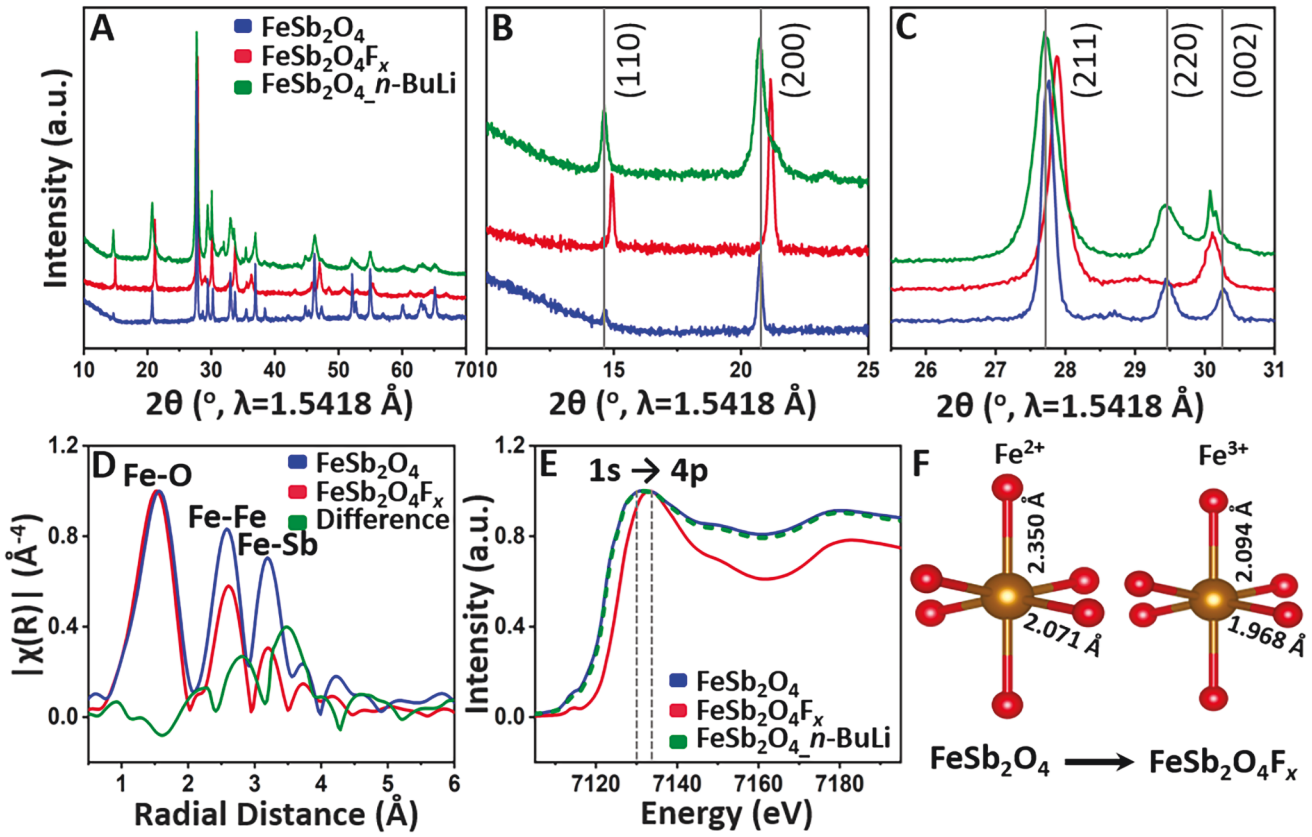

Figure 2. Structural characterization of $FeSb_2O_4$ upon fluoridation. (A) Comparison of powder X-ray diffraction data collected for $FeSb_2O_4$, $FeSb_2O_4F_x$ ($x \approx 1$), and $FeSb_2O_4$ recovered after treatment with *n*-butyllithium. Expanded views showing evolution of (B) the (110) and (200) reflections and (C) the (211), (220), and (002) reflections across the F-ion insertion and deinsertion reactions. (D) Normalized k^3-weighted Fourier-transformed R-space data extracted from Fe K-edge EXAFS spectra for $FeSb_2O_4$ and $FeSb_2O_4F_x$ ($x \approx 1$) alongside their difference spectrum. (E) Comparison of normalized Fe K-edge XANES spectra for $FeSb_2O_4$, $FeSb_2O_4F_x$ ($x \approx 1$), and $FeSb_2O_4$ recovered after treatment with *n*-butyllithium. (F) FeO_6 models generated from fitted EXAFS data for $FeSb_2O_4$ and $FeSb_2O_4F_x$ (gold for Fe and red for O).

$FeSb_2O_4$ particles, which are crystallized in a faceted rodlike morphology with diameters ranging from 300 to 500 nm and spanning 1−2 μm in length with some platelets discernible at the edges of the facets.

Topochemical F-ion insertion has been achieved by stirring the hydrothermally synthesized $FeSb_2O_4$ particles with a molar excess of XeF_2 in acetonitrile at 23 °C as per

$$FeSb_2O_4(s) + \frac{x}{2}XeF_2(\text{acetonitrile}) \rightarrow FeSb_2O_4F_x(s) + \frac{x}{2}Xe(g) \quad (2)$$

XeF_2 is a powerful fluoridating agent, which by dint of its high solubility in organic solvents enables a high local chemical activity of F-ion precursors to be established at the solid−liquid interface.[15] In comparison to analogous inorganic salts in which the cation can act as an undesirable secondary intercalant,[14] XeF_2 provides a clean source of F ions, enabling unambiguous characterization of the inserted products (Figure 1). Such a solution-phase fluoridation route further represents a powerful means of evaluating F-ion insertion/extraction and diffusion within solids without necessitating identification of an optimal electrolyte or assembly of a full cell and is analogous to the utilization of alkyllithium compounds in seminal work by Whittingham, which greatly accelerated the discovery of cathode materials for Li-ion batteries.[16]

Rietveld refinement of powder X-ray diffraction (XRD) data collected for the sample fluoridated at room temperature corresponded to a nominal stoichiometry (x) of 1 ± 0.05 in $FeSb_2O_4F_x$, albeit considerable disorder is observed in F-ion sites (Table S2). Comparison of powder XRD patterns collected for the fluoridated and pristine $FeSb_2O_4$ in Figure 2A reveals preservation of tetragonal symmetry across the topochemical reaction but with some notable changes. The reflections from the (002) planes appear at lower 2θ values compared to the reflections from the (220) planes, and the reflections from the (112) planes are shifted to lower 2θ values compared to the reflections from the (310) planes (Figure 2B,C), suggesting an anisotropic expansion of the tunnel such that the SbO_3 polyhedra are buckled inward and the FeO_6 octahedra are pressed outward as shown in Figure 1 and Figure S1.

An 80 °C treatment allows the F ions to be situated in the lowest-energy interstitial sites. Figure S4 shows powder XRD data and its refinement that allows for identification of the F-ion crystallographic sites within the tunnel as shown in Figure 1 and Figure S1 (Tables S3 and S4). The tunnels serve as channels for diffusion of F ions between interstitial sites bounded by Sb atoms. Overall, F-ion insertion induces a very modest contraction (<1%) in going from $FeSb_2O_4$ to $FeSb_2O_4F_x$ ($x \approx 1$); the observed lattice contraction manifests the consequences of oxidative insertion. As expected from the analysis of the powder XRD patterns, the a and b lattice parameters decrease upon F-ion insertion, whereas the parameter c increases. The position of F ions is slightly off-center from the tetrahedral site created by four Sb atoms as depicted in Figure 1 and Figure S1.

https://dx.doi.org/10.1021/acsenergylett.0c01328
ACS Energy Lett. 2020, 5, 2520−2526

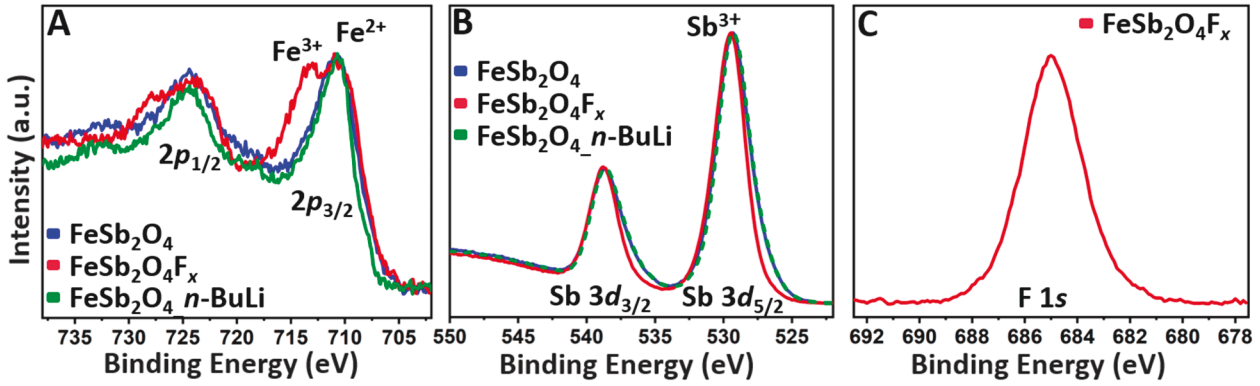

Figure 3. Electronic structure spectroscopy of $FeSb_2O_4$ before and after F-ion insertion. High-resolution HAXPES plots for (A) Fe 2p and (B) Sb 3d core excitations collected for $FeSb_2O_4$, $FeSb_2O_4F_x$ ($x \approx 1$), and $FeSb_2O_4$ recovered after treatment of $FeSb_2O_4F_x$ with *n*-butyllithium. (C) F 1s core excitations for $FeSb_2O_4F_x$ ($x \approx 1$).

This local distortion is indicative of stabilization of F ions as a result of the preferred coordination to one of the four Sb atoms. Changes in the average structure of $FeSb_2O_4$ as a result of fluoridation and observed through diffraction are visualized in Videos S1 and S2.

Modifications of the local atomistic structure as a result of fluoridation have been further investigated using extended X-ray absorption fine structure (EXAFS) spectroscopy collected at the Fe K edge. Shell fitting for EXAFS data has been performed starting from the atomic coordinates obtained from Rietveld refinements of the powder XRD data. Fourier-transformed R-space EXAFS data for $FeSb_2O_4$, $FeSb_2O_4F_x$ ($x \approx 1$), and their difference are plotted in Figure 2D. Three prominent features are assigned as follows: the correlation at approximately 2.1 Å is fitted to Fe−O_{eq} (equatorial) and Fe−O_{ax} (axial) paths; the correlation at approximately 3.0 Å is attributed to the Fe−Fe separation; and the feature at approximately 3.5 Å is assigned to an Fe−Sb path. Upon fluoridation, the Fe−O bonds are significantly decreased in length. The Fe−$O_{ax.}$ bond lengths decrease from 2.350 to 2.094 Å, whereas the Fe−O_{eq} bond distances decrease from 2.071 to 1.968 Å, reflective of oxidation of divalent iron to trivalent iron. Figure 2F shows models of FeO_6 octahedra constructed using the Fe−O distances derived from fitting the EXAFS data in Figures S5—S7 (Tables S5 and S6). The local structure data are in excellent agreement with the average structure gleaned from analysis of the powder XRD data but further delineate the local distortions of the FeO_6 coordination environment as a result of oxidative F-ion insertion.

To investigate the reversibility of the F-ion insertion, which is necessary for use in an insertion-type F-ion battery, the $FeSb_2O_4F_x$ material was reacted with a strong reducing agent, *n*-butyllithium in hexanes (Figure 1), at 23 °C as per

$$FeSb_2O_4F_x(s) + xC_4H_9Li(\text{hexane}) \rightarrow FeSb_2O_4(s) + xLiF(s) + \frac{x}{2}C_8H_{18}(l) \quad (3)$$

Remarkably, the pristine $FeSb_2O_4$ phase was recovered as the primary product. The LiF byproduct that forms as a result was removed by subsequent washing and centrifugation. Following the reaction with *n*-butyllithium, the lattice was returned to its original state. A powder XRD pattern obtained for the deinserted sample is presented in Figure 2A. The refined lattice parameters [$a = b = 8.5684(9)$ Å, and $c = 5.9315(12)$ Å] suggest the near-complete removal of F ions from the lattice (Table S7) and show a recovery of the undistorted $FeSb_2O_4$ crystal lattice. Indeed, the spectra obtained by X-ray absorption near-edge spectroscopy (XANES) analysis at the Fe K edge of the pristine $FeSb_2O_4$ and the F-ion deintercalated sample in Figure 2E are nearly superimposable, indicating quantitative deinsertion within the limits of detection. The Fe−O bond distances deduced from the fitting of EXAFS data are further recovered upon deinsertion of F ions with *n*-butyllithium with Fe−O_{eq} and Fe−O_{ax} distances of 2.060 and 2.340 Å, respectively. The facile deinsertion of the F ions at room temperature attests to the reversibility of the solution-phase F-ion insertion reaction for submicrometer-sized $FeSb_2O_4$ particles and is further evidence of the facile solid-state diffusion of F ions across hundreds of nanometers within this material.

X-ray absorption and emission spectroscopies have been used to probe the electronic structure of $FeSb_2O_4$ across the F-ion insertion and deinsertion reactions. Analysis of the Fe K-edge XANES spectra in Figure 2E reveals that the primary absorption feature, which is attributed to an Fe 1s → Fe 4p transition, is shifted from approximately 7130 eV in $FeSb_2O_4$ to approximately 7133 eV in $FeSb_2O_4F_x$, indicative of the oxidation of divalent iron to trivalent iron (i.e., $x \approx 1$).[17] F K-edge XANES measurements in Figure S8A further confirm the insertion of ionic fluoride species in $FeSb_2O_4$.[18] On the basis of the relative ratios of Fe L_{III} and Fe L_{II} features in the Fe L-edge XANES spectrum in Figure S8A, a trivalent oxidation state can be inferred for the iron centers after F-ion insertion.[19] The oxidation of Fe underpins the shrinkage of Fe−O bonds observed in the EXAFS measurements and is further consistent with an increased Fe−Fe distance manifested as an increase in the *c* parameter measured by powder XRD.

Contiguous Sb M-edge and O K-edge XANES spectra for $FeSb_2O_4$ and $FeSb_2O_4F_x$ ($x \approx 1$) are shown in Figure S8B. Because Sb atoms have a trigonal-pyramidal geometry in $FeSb_2O_4$, a strong pre-edge feature is observed that is derived from a transition from Sb $3d_{3/2}$ core levels to Sb 5s hybridized states in the conduction band. The primary absorption feature at the Sb M_{IV} edge arises from a Sb $3d_{3/2}$ → Sb 5p transition. The two features are not shifted in energy upon F-ion insertion, consistent with the redox event primarily being centered on the iron centers. The modulation of intensity at the pre-edge derives from a distortion of the local coordination geometry of Sb from a formally trigonal pyramidal SbO_3 to an expanded quasi-tetrahedral SbO_3F motif upon F-ion insertion (Figure 1),

https://dx.doi.org/10.1021/acsenergylett.0c01328
ACS Energy Lett. 2020, 5, 2520−2526

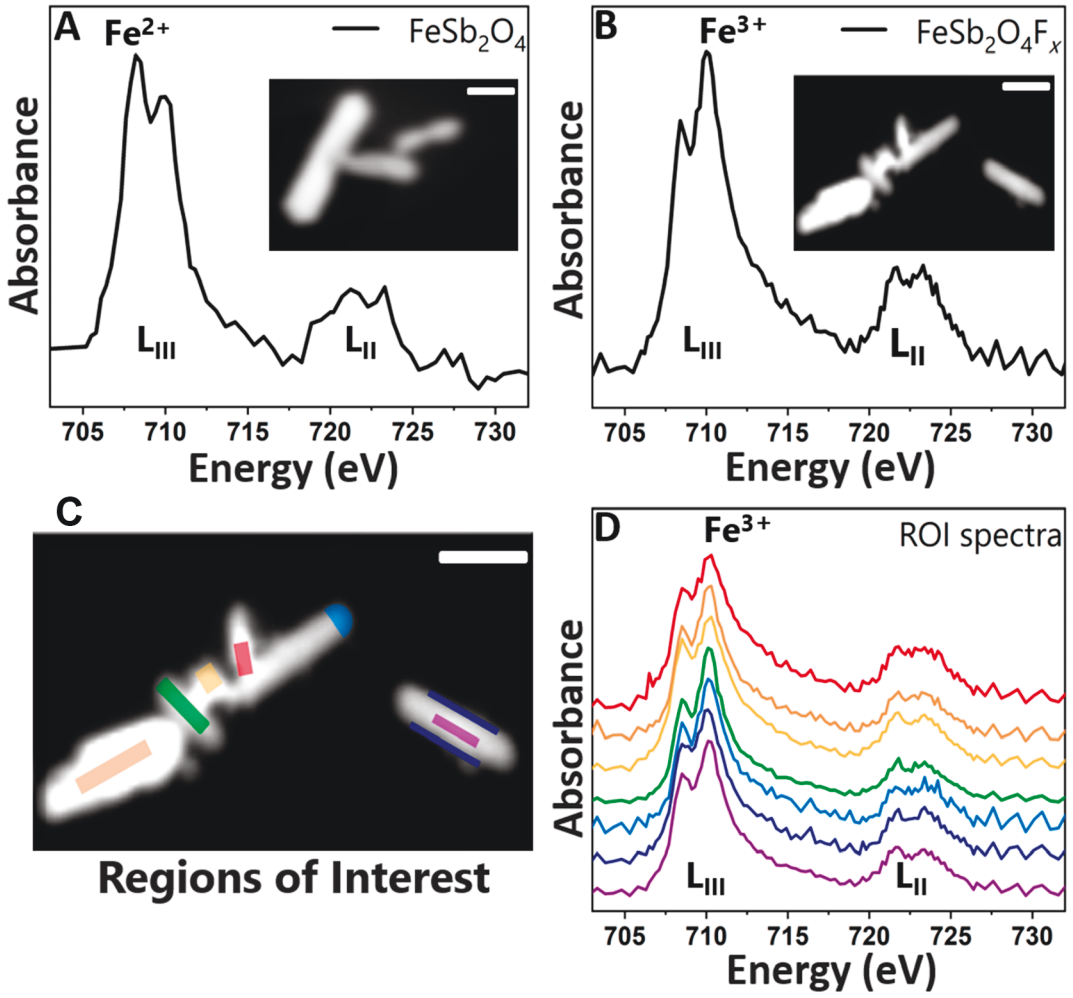

Figure 4. Mapping inter- and intraparticle homogeneity of F-ion insertion in $FeSb_2O_4$. (A) Fe $L_{III,II}$-edge X-ray absorption spectrum obtained for $FeSb_2O_4$ rods by integrating across the entire region shown in the inset STXM image (scale bar, 500 nm). (B) Fe $L_{III,II}$-edge X-ray absorption spectrum obtained for $FeSb_2O_4F_x$ ($x \approx 1$) rods by integrating across the entire region shown in the inset STXM image (scale bar, 1 μm). (C) Spatially resolved regions of interest corresponding to the data shown in panel D (scale bar, 1 μm). (D) Color-coded Fe L-edge spectra corresponding to the regions highlighted in panel C.

which further corroborates the positioning of F ions within the tunnels of the structure gleaned from diffraction measurements. Quantitative oxidation of Fe centers is achieved within the limits of detection, which portend high Coulombic efficiencies if an appropriate electrolyte can be paired with this material.

To further prove that fluoridation is not a surface phenomenon, hard X-ray photoelectron spectroscopy (HAXPES) measurements were performed for the pristine, F-ion-inserted, and defluoridated $FeSb_2O_4$ materials (Figure 3). The high incident photon energy of HAXPES increases the kinetic energy of the emitted electron and hence its mean free path, enabling interrogation of the bulk electronic structure of the material.[20] Figure 3A provides unambiguous evidence of the oxidation of iron centers beyond the surface into the bulk of the material. A distinctive feature characteristic of Fe centers with a +3 formal oxidation state emerges at a higher binding energy of 713 eV in high-resolution Fe $2p_{3/2}$ spectra upon F-ion insertion.[21] Treatment with *n*-butyllithium reduces the iron centers back to a lower formal oxidation state of +2 and is accompanied by the concomitant removal of F ions, attesting to the reversibility of the process at room temperature. The Sb 3d high-resolution HAXPES spectra in Figure 3B show a Sb $3d_{5/2}$ peak centered at approximately 530 eV for $FeSb_2O_4$, which corresponds to the +3 oxidation formal state for Sb. No discernible oxidation is observed, further corroborating that the redox reaction is centered on the iron atoms. F-ion deinsertion yields a Sb 3d HAXPES spectrum that can be practically superimposed with the pristine sample, once again confirming near quantitative defluoridation. Figure 3C shows a F 1s HAXPES spectrum acquired for $FeSb_2O_4$ ($x \approx 1$), which is further consistent with F-ion insertion within the bulk of the material. Figure S9 contrasts the density of states calculated by density functional theory for $FeSb_2O_4$ and its fluoridated counterpart. The atom-projected density of states plots indicate that Fe−O hybrid states lie at the top of the valence band, higher in energy than the Sb−O states, and are thus preferentially oxidized upon F-ion insertion. Upon oxidation, Fe 3d−O 2p hybrid states appear at the bottom of the conduction band. The newly stabilized Sb−F states reside at the valence band maximum in $FeSb_2O_4F$. These Sb−F lone pair states are higher in energy than the Sb−O states, and therefore, the Sb centers retain their formally trivalent oxidation state. The low-lying conduction band states and the diminished bandgap are expected to enable electronic conductivity. The X-ray

https://dx.doi.org/10.1021/acsenergylett.0c01328
ACS Energy Lett. 2020, 5, 2520−2526

absorption and emission measurements thus evidence bulk F-ion insertion and reveal that oxidation and reduction are highly reversible and occur at the iron centers.

In addition to ensemble spectroscopy measurements, scanning transmission X-ray microscopy (STXM) has been performed at the Fe L edge to probe the homogeneity of F-ion insertion across and within individual $FeSb_2O_4$ particles, which is analogous to the approach used to study lithiation gradients in Li_xFePO_4 and other battery electrodes.[19,22,23] Panels A and B of Figure 4 show integrated STXM spectra and optical density images (inset) collected at the Fe L edge for $FeSb_2O_4$ and $FeSb_2O_4F_x$ ($x \approx 1$) rods suspended on X-ray transparent silicon nitride windows. The Fe L_{III}-edge spectrum for pristine $FeSb_2O_4$ (Figure 4A) has a predominant feature centered at approximately 708 eV, whereas the predominant absorption feature for $FeSb_2O_4F_x$ ($x \approx 1$) is shifted to approximately 710 eV. These energy features can be assigned to formal oxidation states of +2 and +3 in iron, respectively.[19] Because STXM spectra are recorded in transmission mode and therefore probe the entire depth of the material, the data further attest to bulk insertion of F ions. In other words, STXM imaging evidences oxidation of iron centers concomitant with F-ion insertion. The spatially resolved region-of-interest analysis in panels C and D of Figure 4 highlights the striking homogeneity of oxidation of Fe centers across different particles (red, green, and orange regions) and within individual particles (blue and purple regions), which resolves issues with almost entirely surficial F-ion diffusion, which has plagued electrode materials of F-ion conversion batteries.[8,10−12]

In conclusion, we have demonstrated the unprecedented reversible insertion and bulk diffusion of F ions from solution at room temperature in micrometer-sized $FeSb_2O_4$ particles with full preservation of the crystalline host lattice. The use of XeF_2 as a fluoridating agent results in a high degree of fluoridation with $x \approx 1$ in $FeSb_2O_4$, corresponding to a F ion for each redox active Fe atom; F-ion insertion oxidizes iron centers from +2 to +3 and is observed to proceed homogeneously across the micrometer-sized particles. Room-temperature treatment with *n*-butyllithium extracts the inserted F ions, reduces trivalent iron back to divalent centers, and restores the pristine $FeSb_2O_4$ structure. The structural reversibility of $FeSb_2O_4$ upon F-ion insertion/deinsertion and the <1% change in volume (which is in stark contrast to massive volume changes evidenced in F-ion conversion-type batteries)[11] derive from the rigidity of large one-dimensional channels bounded by SbO_3 trigonal pyramids. F ions are coordinated in the proximity of a pair of Fe and Sb sites, inducing an anisotropic contraction of the tunnel. The elucidation of lattice distortions, interstitial sites, and site-selective redox accomplished here provides design principles for the discovery of insertion electrodes for F-ion batteries and provides a benchmark insertion electrode to guide electrolyte design. The first demonstration of the use of XeF_2 and *n*-butyllithium as a robust means of topochemically screening F-ion insertion electrodes represents a significant step toward enabling evaluation of next-generation anion battery materials without building a full cell. Future work will focus on elucidation of the synergy between iron and antimony centers that enables unprecedented room-temperature F-ion insertion, reversible deinsertion, and bulk diffusion in this material.

■ ASSOCIATED CONTENT

Supporting Information

The Supporting Information is available free of charge at https://pubs.acs.org/doi/10.1021/acsenergylett.0c01328.

Structural depictions of $FeSb_2O_4$ and $FeSb_2O_4F$, SEM and TEM images, Rietveld refinements to powder XRD data, Fe K-edge EXAFS fits, XANES data for the O K edge, Sb M edge, F K edge, and Fe L edge, calculated density of states plot, and experimental methods (PDF)

Video S1 (AVI)

Video S2 (AVI)

■ AUTHOR INFORMATION

Corresponding Author

Sarbajit Banerjee − *Department of Chemistry and Department of Material Science and Engineering, Texas A&M University, College Station, Texas 77845-3012, United States;* orcid.org/0000-0002-2028-4675; Email: banerjee@chem.tamu.edu

Authors

Wasif Zaheer − *Department of Chemistry and Department of Material Science and Engineering, Texas A&M University, College Station, Texas 77845-3012, United States; Advanced Light Source, Lawrence Berkeley National Laboratory, Berkeley, California 94720, United States*

Justin L. Andrews − *Department of Chemistry and Department of Material Science and Engineering, Texas A&M University, College Station, Texas 77845-3012, United States*

Abhishek Parija − *Department of Chemistry and Department of Material Science and Engineering, Texas A&M University, College Station, Texas 77845-3012, United States; Advanced Light Source, Lawrence Berkeley National Laboratory, Berkeley, California 94720, United States*

Forrest P. Hyler − *Department of Chemistry, University of California, Davis, Davis, California 95616, United States*

Cherno Jaye − *Material Measurement Laboratory, National Institute of Standards and Technology, Gaithersburg, Maryland 20899, United States*

Conan Weiland − *Material Measurement Laboratory, National Institute of Standards and Technology, Gaithersburg, Maryland 20899, United States*

Young-Sang Yu − *Advanced Light Source, Lawrence Berkeley National Laboratory, Berkeley, California 94720, United States*

David A. Shapiro − *Advanced Light Source, Lawrence Berkeley National Laboratory, Berkeley, California 94720, United States*

Daniel A. Fischer − *Material Measurement Laboratory, National Institute of Standards and Technology, Gaithersburg, Maryland 20899, United States*

Jinghua Guo − *Advanced Light Source, Lawrence Berkeley National Laboratory, Berkeley, California 94720, United States;* orcid.org/0000-0002-8576-2172

Jesús M. Velázquez − *Department of Chemistry, University of California, Davis, Davis, California 95616, United States;* orcid.org/0000-0003-2790-0976

Complete contact information is available at: https://pubs.acs.org/10.1021/acsenergylett.0c01328

Notes

The authors declare no competing financial interest.

https://dx.doi.org/10.1021/acsenergylett.0c01328
ACS Energy Lett. 2020, 5, 2520−2526

■ ACKNOWLEDGMENTS

This work was primarily supported by the National Science Foundation under DMR 1809866. The research was funded in part by Grant A-1978-20190330 from the Welch Foundation. J.M.V. acknowledges the University of California, Davis for start-up funding for this work, as well as support from the Cottrell Scholar program supported by the Research Corporation for Science Advancement (RCSA Grant 26780). W.Z. and A.P. acknowledge support from the Advanced Light Source (ALS) doctoral fellowship in residence. The Advanced Light Source is supported by the Director, Office of Science, Office of Basic Energy Sciences, of the U.S. Department of Energy (DOE), under Contract DE-AC02-05CH11231. This research used resources of the National Synchrotron Light Source II, a U.S. Department of Energy (DOE) Office of Science User Facility operated for the DOE Office of Science by Brookhaven National Laboratory under Contract DE-SC0012704. Use of the Stanford Synchrotron Radiation Lightsource, SLAC National Accelerator Laboratory, is supported by the DOE, Office of Science, Office of Basic Energy Sciences, under Contract DE-AC02-76SF00515. J.L.A. acknowledges support from a NASA Space Technology Research Fellowship under Grant 80NSSC17K0182. The TAMU Materials Characterization Facility is acknowledged. Use of the TAMU Microscopy and Imaging Center is acknowledged. DFT simulations were performed as part of a User Project at The Molecular Foundry (TMF), Lawrence Berkeley National Laboratory. The Molecular Foundry is supported by the Office of Science, Office of Basic Energy Sciences, of the DOE, under Contract DE-AC02-05CH11231. Portions of this research were conducted with the advanced computing resources provided by Texas A&M High Performance Research Computing.

■ REFERENCES

(1) Myung, S. T.; Maglia, F.; Park, K. J.; Yoon, C. S.; Lamp, P.; Kim, S. J.; Sun, Y. K. Nickel-Rich Layered Cathode Materials for Automotive Lithium-Ion Batteries: Achievements and Perspectives. *ACS Energy Lett.* **2017**, *2* (1), 196−223.

(2) Goodenough, J. B.; Park, K. S. The Li-Ion Rechargeable Battery: A Perspective. *J. Am. Chem. Soc.* **2013**, *135* (4), 1167−1176.

(3) Konarov, A.; Voronina, N.; Jo, J. H.; Bakenov, Z.; Sun, Y. K.; Myung, S. T. Present and Future Perspective on Electrode Materials for Rechargeable Zinc-Ion Batteries. *ACS Energy Lett.* **2018**, *3* (10), 2620−2640.

(4) Andrews, J. L.; Mukherjee, A.; Yoo, H. D.; Parija, A.; Marley, P. M.; Fakra, S.; Prendergast, D.; Cabana, J.; Klie, R. F.; Banerjee, S. Reversible Mg-Ion Insertion in a Metastable One-Dimensional Polymorph of V_2O_5. *Chem.* **2018**, *4* (3), 564−585.

(5) Yadav, G. G.; Turney, D.; Huang, J.; Wei, X.; Banerjee, S. Breaking the 2 V Barrier in Aqueous Zinc Chemistry: Creating 2.45 and 2.8 V MnO_2-Zn Aqueous Batteries. *ACS Energy Lett.* **2019**, *4* (9), 2144−2146.

(6) Wang, N.; Chu, C.; Xu, X.; Du, Y.; Yang, J.; Bai, Z.; Dou, S. Comprehensive New Insights and Perspectives into Ti-Based Anodes for Next-Generation Alkaline Metal (Na^+, K^+) Ion Batteries. *Adv. Energy Mater.* **2018**, *8* (27), 1801888.

(7) Gu, S.; Wang, H.; Wu, C.; Bai, Y.; Li, H.; Wu, F. Confirming Reversible Al^{3+} Storage Mechanism through Intercalation of Al^{3+} into V_2O_5 Nanowires in a Rechargeable Aluminum Battery. *Energy Storage Mater.* **2017**, *6*, 9−17.

(8) Anji Reddy, M.; Fichtner, M. Batteries Based on Fluoride Shuttle. *J. Mater. Chem.* **2011**, *21* (43), 17059−17062.

(9) Gschwind, F.; Rodriguez-Garcia, G.; Sandbeck, D. J. S.; Gross, A.; Weil, M.; Fichtner, M.; Hörmann, N. Fluoride Ion Batteries: Theoretical Performance, Safety, Toxicity, and a Combinatorial Screening of New Electrodes. *J. Fluorine Chem.* **2016**, *182*, 76−90.

(10) Okazaki, K. I.; Uchimoto, Y.; Abe, T.; Ogumi, Z. Charge-Discharge Behavior of Bismuth in a Liquid Electrolyte for Rechargeable Batteries Based on a Fluoride Shuttle. *ACS Energy Lett.* **2017**, *2* (6), 1460−1464.

(11) Thieu, D. T.; Fawey, M. H.; Bhatia, H.; Diemant, T.; Chakravadhanula, V. S. K.; Behm, R. J.; Kübel, C.; Fichtner, M. CuF_2 as Reversible Cathode for Fluoride Ion Batteries. *Adv. Funct. Mater.* **2017**, *27* (31), 1701051.

(12) Davis, V. K.; Bates, C. M.; Omichi, K.; Savoie, B. M.; Momčilović, N.; Xu, Q.; Wolf, W. J.; Webb, M. A.; Billings, K. J.; Chou, N. H.; et al. Room-Temperature Cycling of Metal Fluoride Electrodes: Liquid Electrolytes for High-Energy Fluoride Ion Cells. *Science* **2018**, *362* (6419), 1144−1148.

(13) De Laune, B. P.; Rees, G. J.; Marco, J. F.; Hah, H. Y.; Johnson, C. E.; Johnson, J. A.; Berry, F. J.; Hanna, J. V.; Greaves, C. Topotactic Fluorine Insertion into the Channels of $FeSb_2O_4$-Related Materials. *Inorg. Chem.* **2017**, *56* (16), 10078−10089.

(14) Nowroozi, M. A.; Wissel, K.; Rohrer, J.; Munnangi, A. R.; Clemens, O. $LaSrMnO_4$: Reversible Electrochemical Intercalation of Fluoride Ions in the Context of Fluoride Ion Batteries. *Chem. Mater.* **2017**, *29* (8), 3441−3453.

(15) Ramsden, C. A. Xenon Difluoride in the Organic Laboratory: A Tale of Substrates, Solvents and Vessels. *Arkivoc* **2013**, *2014* (1), 109−126.

(16) Whittingham, M. S.; Martin, B. D. *n*-Butyllithium—An Effective, General Cathode Screening Agent. *J. Electrochem. Soc.* **1977**, *124* (9), 1387.

(17) Wang, J.; Yang, J.; Tang, Y.; Li, R.; Liang, G.; Sham, T. K.; Sun, X. Surface Aging at Olivine $LiFePO_4$: A Direct Visual Observation of Iron Dissolution and the Protection Role of Nano-Carbon Coating. *J. Mater. Chem. A* **2013**, *1* (5), 1579−1586.

(18) Murugesan, V.; Cho, J. S.; Govind, N.; Andersen, A.; Olszta, M. J.; Han, K. S.; Li, G.; Lee, H.; Reed, D. M.; Sprenkle, V. L.; et al. Lithium Insertion Mechanism in Iron Fluoride Nanoparticles Prepared by Catalytic Decomposition of Fluoropolymer. *ACS Appl. Energy Mater.* **2019**, *2* (3), 1832−1843.

(19) Ohmer, N.; Fenk, B.; Samuelis, D.; Chen, C. C.; Maier, J.; Weigand, M.; Goering, E.; Schütz, G. Phase Evolution in Single-Crystalline $LiFePO_4$ Followed by in Situ Scanning X-Ray Microscopy of a Micrometre-Sized Battery. *Nat. Commun.* **2015**, *6*, 6045.

(20) Weiland, C.; Rumaiz, A. K.; Pianetta, P.; Woicik, J. C. Recent Applications of Hard X-Ray Photoelectron Spectroscopy. *J. Vac. Sci. Technol., A* **2016**, *34* (3), No. 030801.

(21) Grosvenor, A. P.; Kobe, B. A.; Biesinger, M. C.; McIntyre, N. S. Investigation of Multiplet Splitting of Fe 2p XPS Spectra and Bonding in Iron Compounds. *Surf. Interface Anal.* **2004**, *36* (12), 1564−1574.

(22) De Jesus, L. R.; Stein, P.; Andrews, J. L.; Luo, Y.; Xu, B. X.; Banerjee, S. Striping Modulations and Strain Gradients within Individual Particles of a Cathode Material upon Lithiation. *Mater. Horiz.* **2018**, *5* (3), 486−498.

(23) De Jesus, L. R.; Andrews, J. L.; Parija, A.; Banerjee, S. Defining Diffusion Pathways in Intercalation Cathode Materials: Some Lessons from V_2O_5 on Directing Cation Traffic. *ACS Energy Lett.* **2018**, *3* (4), 915−931.

https://dx.doi.org/10.1021/acsenergylett.0c01328
ACS Energy Lett. 2020, 5, 2520−2526